Multichannel multimodal piezoelectric middle ear implant concept based on MEMS technology for next-generation fully implantable cochlear implant applications

Feyza Pirim [a,b,c], Ali Can Atik [a,d], Muhammed Berat Yüksel [a,d], Akın Mert Yılmaz [a,d], Mehmet Birol Uğur [e], Selçuk Tunalı [f], Aykan Batu [d], Mahmut Kamil Aslan [a], Mehmet Bülent Özer [c], Haluk Külah [a,b,d,*]

[a] METU MEMS Research and Application Center, Middle East Technical University, Turkey
[b] Department of Micro and Nanotechnology, Middle East Technical University, Turkey
[c] Department of Mechanical Engineering, Middle East Technical University, Turkey
[d] Department of Electrical and Electronics Engineering, Middle East Technical University, Turkey
[e] Faculty of Medicine, Gazi University, Turkey
[f] Faculty of Medicine, TOBB University of Economics and Technology, Turkey

ARTICLE INFO

ABSTRACT

This paper introduces a unique multimode, multichannel piezoelectric vibration sensor for the next-generation fully implantable cochlear implant (FICI) systems. The sensor, which can be implanted on the middle ear chain to collect and filter the ambient sound in eight frequency bands, comprises an array of 4 M-shape multimode and 11 single cantilevers. Finite element (FE) analysis indicates a 2.05-fold improvement in capturing frequency information for the multimodal sensor compared to its single-mode counterpart. Under an acoustic excitation at 100 dB SPL, the sensor, mounted on an artificial tympanic membrane, yielded a peak output voltage of 546.16 mVpp and a peak sensitivity of 285.28 mVpp/Pa at 1613 Hz. The extrapolated acoustic results indicated a dynamic frequency range between 300 Hz and 6 kHz, even at 30 dB SPL. Furthermore, a lightweight titanium coupler, employing a two-sided clipping structure with a maximum wall thickness of 70 μm, is micromachined for surgical attachment of the transducer to the middle ear chain. A commercial accelerometer, implanted on the incus short process (SP) of a cadaver using the titanium coupler, successfully recorded 0.1 g for 100 dB SPL at 500 Hz, revealing the potential feasibility of the coupler for vibration sensor implantation. Moreover, the presented anatomically accurate FE model of the middle ear, exhibiting a high correlation coefficient (R^2) of 0.97 with the cadaveric experiment, suggests an efficient numerical approach for evaluating the implantation of middle ear prostheses. In this regard, the study holds great promise for clinical application in the field of implantable hearing aids.

1. Introduction

The hearing function of the human ear is crucial to information exchange; thus, hearing loss could significantly decrease the quality of everyday life regarding socio-emotional and socio-economic well-being as a communication disorder. Unfortunately, the World Health Organization (WHO) forecasts that approximately 2.5 billion people will have varying degrees of hearing loss by 2050, and at least 700 million will need hearing rehabilitation (Chadha et al., 2021). Sensorineural

impairment is the most common type of hearing loss and results from irreversible damage to the hair cells inside the cochlea, thereby leading to a permanent reduction or loss of hearing sensitivity. The standard therapeutic solutions for moderate to profound sensorineural hearing loss are cochlear implants (CIs), which target the inner ear to stimulate the auditory nerve electrically (Saunders et al., 2016; Wilson and Dorman, 2008; Wyatt et al., 1995). Conventional CIs typically incorporate an external microphone, a speech processor, an electrode array, a transmitter, and a stimulator. However, most clinically available CIs

have significant drawbacks, such as cumbersome wear of delicate external components, complex signal processing steps, daily battery recharge requirements, and aesthetic concerns. In recent years, self-powered, autonomous, and fully implantable cochlear implant systems have been suggested to eliminate these drawbacks.

In the FICI concept, typically, an implantable transducer converts vibrations of the incoming sound into electrical signals, which are then utilized to stimulate the auditory nerves inside the cochlea through an electrode array. Advances in micro-electromechanical systems (MEMS) have enabled the development of emerging FICI concepts through capacitive, piezoresistive, and piezoelectric sensor technologies. For instance, a capacitive accelerometer is developed to be used as a middle ear microphone attached to the umbo, and the system/sensor has a sound detection level of 60 dB at 500 Hz, 35 dB at 2 kHz, and 57 dB at 8 kHz (Young et al., 2012). In another study, a MEMS-based capacitive displacement sensor is proposed, with a sound detection performance above 40 dB SPL in a frequency range from 500 Hz to 5 kHz (Ko et al., 2009a). The piezoelectric energy conversion mechanism stands out thanks to its several advantages for biosensor applications (Zhao et al., 2023), including compatibility with microfabrication methods, self-powered characteristics, high energy density, and high voltage generation capability. For example, an Aluminum Nitride (AlN) piezoelectric accelerometer coupled to the ossicular chain is presented, which results in a functional bandwidth between 600 Hz and 10 kHz for lower than 60 dB SPL (Gesing et al., 2018). In another study, a lead zirconate titanate (PZT)-based microphone encapsulated in titanium packaging is developed, which detects 50 dB SPL between 500 Hz and 8.0 kHz (Jia et al., 2016). These sensors mentioned above discern a narrower frequency band by delimiting band edges as the input sound pressure level decreases, so they exhibit a reduced operating frequency range at low excitation levels. Where a single sensor may not be sufficient to capture all the necessary information, multichannel sensor systems, as a pre-eminent solution, address this limitation by integrating multiple channels into a single unit, allowing for the collection of more diverse data simultaneously in the frequency range of interest. At this point, artificial basilar membrane prototypes, composed of a piezoelectric cantilever array (Jang et al., 2015) or beam array (Jang et al., 2013), are introduced to enhance the frequency range. Despite having multiple channels, both devices exhibit inferior selectivity at fundamental frequency tones below kHz-regime, which have crucial importance over the hearing quality.

Previously, our research group developed a bulk PZT-based harvester, where one cantilever has a footprint of 4.25 mm × 4 mm, which is unsuitable for an array configuration for energy-efficient mechanical filtering of incoming sound (Beker et al., 2013). The actualization of cantilever arrays is enabled via thin-film deposition of pulsed laser-deposited (PLD) PZT (İlik et al., 2018; Yuksel et al., 2022). Although an 8-channel linear cantilever sensor array configuration allows output voltage up to 50.7 mVpp under 100 dB SPL at 652 Hz during in vitro experiments under acoustic input and does not require a control circuit for frequency selectivity, a significant part of the operation frequency interval is missing, especially at lower sound pressure levels (Yuksel et al., 2022). A practical solution is to increase the number of resonances to detect more frequency information in the intended range, even under low-excitation scenarios. Here, multimodal sensors, with multiple resonant modes for interacting with the excitation, provide enhanced functionality and versatility compared to single-mode cantilever beams by allowing for a more compact design, reducing space requirements, and simplifying integration into systems (Masara et al., 2021; Wu et al., 2015). Compact multimodal structures can efficiently capture a broader range of frequencies by having multiple modes, increasing overall energy conversion efficiency. This paper proposes a new multichannel and multimodal MEMS-based piezoelectric vibration sensor, incorporating asymmetric three-mode M-shaped beams to obtain a wide dynamic frequency range while gathering ossicular vibration with high resolution. The sensor, consisting of an array of frequency-tuned 4 M-shape multimode cantilevers and 11 serially connected single cantilevers, is designed to be implanted inside the middle ear cavity through an incus SP coupler (Fig. 1a). Multimodal and multichannel attributes of the sensor permit the detection of mechanical vibrations resulting from incoming sound and the employment of specific resonances to filter and segment the signal into eight distinct frequency bands by inherently mimicking the functionality of the cochlea.

Despite offering effectiveness in capturing vibrations across a broad spectrum of frequencies, the feasibility of sensor implantation directly onto the middle ear chain still needs to be determined. The surgical attachment of the transducer could be challenging due to the risk of insertion trauma, considering the delicate nature of the ossicular chain (Graf et al., 2023; Schraven et al., 2016) and the shift in mechanical harmonic response with respect to middle ear impedance (Rusinek, 2021). The factors, including dimensions of the transducer, selection of the structural material, and attachment site, entail designing a unique coupler structure to support the transducer after implantation. Here, we have developed a micromachined, biocompatible, and lightweight titanium coupler with the flexibility to attach to the incus SP through clipping without the need for crimping, thanks to its two-sided clip structure. The titanium coupler, responsible for clamping, is crucial in transferring vibration energy. Furthermore, the LDV measurements highlight a decrease in acceleration amplitude with a slope of 40 dB per decade as the frequency ranges from 1000 Hz down to 250 Hz (Young et al., 2012), indicating a low acceleration response of the middle ear chain at the lower end of the audible spectrum. Consequently, an initial cadaveric experiment was performed for the feasibility assessment of the incus SP attachment of the titanium coupler, where a commercial accelerometer is affixed onto the coupler to collect vibration data of the incus. The incus SP serves as a strategic anchoring point for clamping, as its posterior location allows for easy accessibility through a simple mastoidectomy. The cadaveric experiment validated that the designed titanium coupler can achieve effective clamping to sense a sufficient acceleration level even at low frequencies while ensuring the integrity of the middle ear structures. This empirical validation is crucial for confirming the effectiveness of our proposed methodology in capturing accurate and reliable vibration data.

Moreover, the existing literature needs more comprehensive human or cadaveric studies for the middle ear implantation of sound detection units; however, the experimental verification of the design iterations has low repeatability due to its complexity and time-consuming nature. This paper also introduces an anatomically accurate numerical model based on finite element (FE) methodology. This model is adapted to inspect the transmission of sound pressure-induced vibrations throughout a titanium coupler with mass loading during the design stage of the transducer. The objective is to provide a more efficient numerical approach for evaluating and optimizing the implantation process of middle ear prostheses. The presented numerical model is validated through comparison with existing experimental studies in the literature, as well as a cadaveric experiment conducted within the scope of this study.

In this paper, the 8-channel multimode piezoelectric cantilever beam array was designed by detailed FEM simulations and realized using MEMS process techniques at a dimensional scale for fitting inside the middle ear. The mechanical vibration response characterization of the fabricated piezoelectric transducer was experimentally evaluated using vibration testing conducted on a shaker table. The audio spectrum coverage of each channel was further analyzed via in vitro acoustic tests by coupling the sensor with an artificial tympanic membrane. To this end, this study presents a novel multimode, multichannel piezoelectric vibration sensor with a high potential to be the next-generation transducer for cochlear implant systems. The sensor operates within a broad range of frequencies found in human speech between 300 and 6000 Hz, with a sufficiently wide dynamic range and high output voltage. In addition to sensor development, a unique titanium coupler was developed for a simple sensor attachment on the ossicular chain. Therefore, this paper introduces a comprehensive procedure to the cochlear
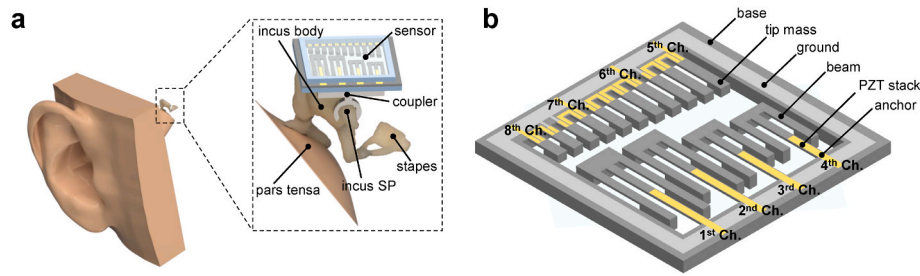
Fig. 1. Representation of middle ear implant concept. (a) Illustration of the system implanted on incus SP. (b) Schematic of multichannel multimodal piezoelectric vibration transducer.

implant literature, which practically covers not only the design and development stages but also the clinical application for the auditory prosthesis.

2. Materials and methods

2.1. MEMS multichannel multimode piezoelectric sensor

Piezoelectric sensors are exceptionally apposite to vibration sensing applications owing to their high voltage generation capability and high sensitivity to the changes to frequency around resonance frequencies in the presence of mechanical input, where no external power source is required. Therefore, the piezoelectric energy transduction mechanism was used to build a vibration sensor to cover the hearing-relevant frequency band of 300–6000 Hz. The multichannel sensor, comprising an array of multimodal cantilever structures, is preferably affixed onto the ossicular chain to sense the frequency of the vibrations of the incoming sound with its mechanical frequency selective structure to stimulate auditory nerves through a subsequent signal processing, stimulation circuit and a conventional cochlear electrode array. Since a part of the natural hearing mechanism was preserved, external units were eliminated, and the power consumption of the system was reduced compared to conventional implants. The design of the sensor unit is a complex process, which details several physical, mechanical, and electrical specifications regarding the objectives and limitations.

The limited volume of the middle ear ($\sim$1 cm^3) restrains the device dimensions (Dahroug et al., 2018; Liem, 2004). Another physical restriction is the mass loading of the ossicles, which affects the vibratory properties of the natural hearing function of the middle ear and induces significant attenuation above 1 kHz (Gan et al., 2001). Based on the developed FE model, considering the limited volume of the middle ear, the physical specifications of the sensor were determined as a footprint of 5 mm–5 mm and weight below 25 mg.

Furthermore, the sensor should be able to supply the minimum voltage level for acoustic pressure levels of everyday speech and environmental sounds (50 dB SPL). Therefore, selecting proper piezoelectric material with high voltage generation capability is essential for obtaining a wide dynamic range and large bandwidth. Thin film piezoelectric materials are relatively easy to integrate with silicon and were preferred over bulk ceramics and single crystals to minimize device size drastically and to enable working with asymmetric geometries. Various thin film piezoelectric materials have been used for piezoelectric acoustic transducers, such as PVDF (Chen et al., 2006; Shintaku et al., 2010), PZT (Beker et al., 2013; Lee et al., 2014), or AlN (Campanella et al., 2012; Jang et al., 2015). In this study, PZT was preferred as piezoelectric material by offering relatively enhanced piezoelectric coefficients for the sensing property of the multimodal multichannel acoustic transducer.

The human voice mainly contains frequencies ranging from 250 Hz to 4 kHz. On the other hand, the upper-frequency range above 4 kHz is important for understanding speech in noisy or complex listening situations (Levy et al., 2015). Hence, the operating frequency range of the sensor is specified to be between 250 Hz and 6 kHz, which corresponds to the most crucial frequency range for speech intelligibility in the human ear with optimal ear responsiveness. In order to extend the working frequency range of the piezoelectric transducers, various methods have been proposed in the literature. For example, wideband operation can be achieved by building a cantilever array structure with different resonance frequencies (Jang et al., 2015; Udvardi et al., 2017; Yuksel et al., 2022). However, in such a structure, every beam has to be excited around its near sole resonance with a narrow bandwidth, which increases the footprint of the sensor. Thus, the array structure will cover the band discretely, while the area normalized total power density will be weakened. Although another way to achieve broadband operation is introducing nonlinearity to the system by adding additional boundary constraints, it is impossible to introduce enough nonlinear deformation to the vibrating structure due to the lower acceleration levels of the middle ear (Nabavi and Zhang, 2017, 2019).

A multiple-mode transducer design can solve low-amplitude and low-frequency scenarios by inducing additional bending modes. Various multimode geometries are adapted to develop sensors for broadband operation, such as M-shape (Leadenham and Erturk, 2014, 2015; Wu et al., 2015), L-shape (Harne et al., 2016; Liu et al., 2018), H-shape (Guan et al., 2013), U-shape (Huang et al., 2021; Sun and Tse, 2019), and other geometries (Nabavi and Zhang, 2017; Udvardi et al., 2017). However, most are not MEMS-based and are studied in large dimensions. Among them, the folded asymmetric M-shaped cantilever structure minimizes the volume while enhancing the operation frequency range by ensuring the first three-order resonances lie in the desired frequency range.

To this end, to cover the frequency range between 300 Hz and 6 kHz, the incipient thin-film PZT-based MEMS vibration sensor comprises 8-channels with multimode operation through an array of 4 M-shaped cantilever structures and 4 serially connected structures of 11 conventional cantilevers (Fig. 1b), operating at lower (below 2.5 kHz) and higher (above 2.5 kHz) bands of human speech bandwidth, respectively. Under base excitation by the sound-driven vibration of the ossicular chain, the beams undergo deflection, resulting in a high stress at the anchored end of the cantilever, where the metal-PZT-metal stack is positioned. The PZT stack undergoes a change in electrical polarization induced by deformation, leading to the accumulation of electric charge across its metal plates, thereby generating a voltage output. The tip mass contributes to adjusting the natural frequency of the structure and capturing more mechanical energy from vibrations. The performance was enhanced by introducing additional mechanically induced resonance peaks at the channel level to meet 50 dB operation requirement with a wider dynamic frequency range. The corresponding resonance modes and the voltage-frequency response curves were obtained by employing COMSOL Multiphysics® v5.6 in response to defined material properties and structural parameters (Supplementary Information Table S5).

2.2. The titanium alloy incus SP coupler

The ossicular chain has variable displacement and force characteristics at each link; as a result, depending on where the transducer is coupled, different dynamic features can be observed. While exploring a range of different coupling conditions in temporal bones, incus vibration characteristics are found to be suitable for coupling by the transducer as well as the placement of the transducer (Young et al., 2010; Zurcher et al., 2006; Gan et al., 2007; Sun et al., 2002; Zhang et al., 2014). The proposed coupler allows one side of the sensor to be securely glued, while the other side is connected to the incus SP with enough tightness, to provide effective transmission of the vibration between the sensor and the ossicular chain. Therefore, a two-sided clipping structure with a thin wall thickness, capable of flexing during implantation due to low stiffness, was preferred. Despite its flexibility, it should exhibit a high material strength to securely wrap around the bone after attachment. The design should also prioritize low mass and a high resonance frequency to effectively mitigate the influences of mass, damping and position misalignment by providing enhanced transmissibility. The introduction of mass loading to the middle ear chain leads to a reduction in its natural frequency and a notable decrease in the amplitude of vibrations, particularly evident in higher frequencies (Gan et al., 2001). A high resonance frequency establishes a rigid coupling with high transmissibility, while minimizing the introduction of additional damping to the system. Thus, even in the presence of misalignment after implantation, the coupler facilitates the ability to sense mechanical vibrations within middle ear, ensuring the generation of an acceptable voltage output from the transducer.

To this end, the implant material with a high degree of biocompatibility should exhibit appropriate stiffness, mechanical strength, abrasion, and corrosion resistance in the tissue environment. Titanium and its alloys are often employed owing to their weight efficiency, high mechanical stability, and tissue contact compatibility of a thin layer of surface oxide (Beutner and Hüttenbrink, 2009). Thus, we chose titanium grade 5 (Ti–6Al–4V), composed of aluminum and vanadium, with 6% and 4% percentages, respectively. Additionally, the titanium alloy, specifically Ti–6Al–4V, met the criteria for materials used in medical devices according to ISO 10993 standards, where its biocompatibility was assessed through diverse techniques and assays (Vu et al., 2016).

The 3D model of the coupler was generated on the computer-aided design (CAD) software Autodesk Fusion 360®, (Fig. 1a). The realization of the coupler structure with difficult-to-machine titanium alloys necessitates non-traditional technologies for microfabrication due to its complex, sub-millimeter, and irregular morphology. Wire electrical discharge machining (EDM) was used to micromachine the coupler from titanium alloy surfaces for a high machining rate and accuracy. This precise cutting technique incorporates a fine single-stranded metal wire heated through electrical sparks and a de-ionized water spraying mechanism to prevent corrosion during the process, permitting the manufacturing of difficult-to-machine metal alloys.

The prototypes of the coupler were manufactured with wire EDM. The final machinable wall thickness of the coupler has been reduced to 70 μm. The optimal design was decided through iterative stress distribution analysis by defining fillets to alleviate stress at critical points during the fabrication. The final physical model of the incus SP coupler brings 6.8 mg mass loading.

2.3. FE model of the middle ear

The human middle ear comprises several structures, including the tympanic membrane (TM), bony ossicles, ligaments, and tendons. Comprehending the vibration characteristics of the middle ear can be challenging due to its intricate nature and frequency-dependent complex modes of motion (Puria et al., 2013). To reproduce the complex ossicular chain movement, the FE modeling has been leveraged as a fundamental mathematical tool to comprehend the vibration

characteristics of the middle ear (Chien et al., 2009; Ferris and Prendergast, 2000; Hato et al., 2003; Nishihara et al., 1993; Nishihara and Goode, 1997; Young et al., 2010; Zhang et al., 2014).

Here, we developed a 3D FE model of the middle ear in ANSYS®, which comprises the dynamic structural analysis of ossicles and tympanic membrane (TM). The geometry of the ossicles, including malleus, incus, and stapes, was constructed from a 3D model based on magnetic resonance images of a human cadaver ear ("3D Ear" by McGill University Auditory Mechanics Laboratory is adapted under CC BY-NC-SA 1.0). The morphology of the TM was modeled as an elliptically shaped membrane composed of four primary zones: pars tensa, pars flaccida, tympanic annulus, and umbo. Fig. 2a illustrates the final 3D model geometry of the human middle ear.

Boundaries of the FE model were specified as ligaments and tendons in Fig. 2b, which are lateral malleolar ligament (LML), anterior malleolar ligament (AML), posterior incudal ligament (PIL), superior incudal ligament (SIL), tensor tympani tendon (TT), stapedial tendon (ST), superior malleolar ligament (SML), stapedial annular ligament (SAL). These boundaries were modeled as one-dimensional linear spring-dashpot elements. The ossicles and TM were considered as isotropic and orthotropic materials, respectively. The Young's modulus and density of the TM, ossicles, and joints were adopted based on the study by (Sun et al., 2002; Zhao et al., 2009). The umbo and malleus were assumed to have no damping, while the pars tensa, pars flaccida, and tympanic annulus had a Rayleigh damping proportional to the mass matrix with a constant of 260 s^{-1}. A Rayleigh damping proportional to the stiffness matrix with a constant of 0.0001 s was defined for the incus and stapes. The Young's modulus of the umbo was assumed to be 1/10 of that tympanic membrane, resulting in the malleus handle and umbo not restricting the vibratory ability of the tympanic membrane. The Poisson's ratio for each part of the middle ear system was employed as 0.3 (Zhao et al., 2009). Finally, the boundary at the tympanic ring was represented as fixed support, and the impedance of the cochlear fluid at the stapes footplate was modeled with five one-dimensional spring-damper elements with an amplitude of 100 N/m and 0.01 Nm/s, respectively. Details about material properties used in the FE model can be found in Table S1 in the supplementary information document.

2.4. The cadaveric study

Validation of the FE model and feasibility of the attachment apparatus was investigated via a cadaveric experiment, in which a fresh-frozen adult cadaver was used. After the thawing procedure, the middle ear was accessed under a brightfield microscope by applying the facial recess method. Surgical implantation of the SP couplers required a simple mastoidectomy to access the middle ear cavity. After mastoidectomy, the temporal bones were immersed in 3% saline to maintain moisture during the experiment.

The experimental setup comprised a waveform generator (KEYSIGHT 33500 B Series), an ER2 insert microphone (Etymotic), a commercial dB meter, and an accelerometer (STM-LSM6DSL). First, the attachment apparatus was placed on the incus SP after mastoidectomy by ensuring the tightness of the coupler with bone cement. The accelerometer was securely attached to the back plate of the coupler, mirroring the typical attachment location for the sensor, using a cyanoacrylate-based adhesive. A frequency-modulated sinusoidal signal, whose amplitude was controlled with the dB meter, was produced by the waveform generator. The controlled signal was transmitted to the ER2 insert microphone, which was positioned 2 mm away from the tympanic membrane inside the ear canal of the cadaver. The tympanic membrane started to vibrate under acoustic input, resulting in the vibration response in the ossicle chain. The vibration data of the incus SP is collected via the accelerometer with an acoustic input of 70 dB–100 dB SPL for a frequency interval of 250 Hz–750 Hz.
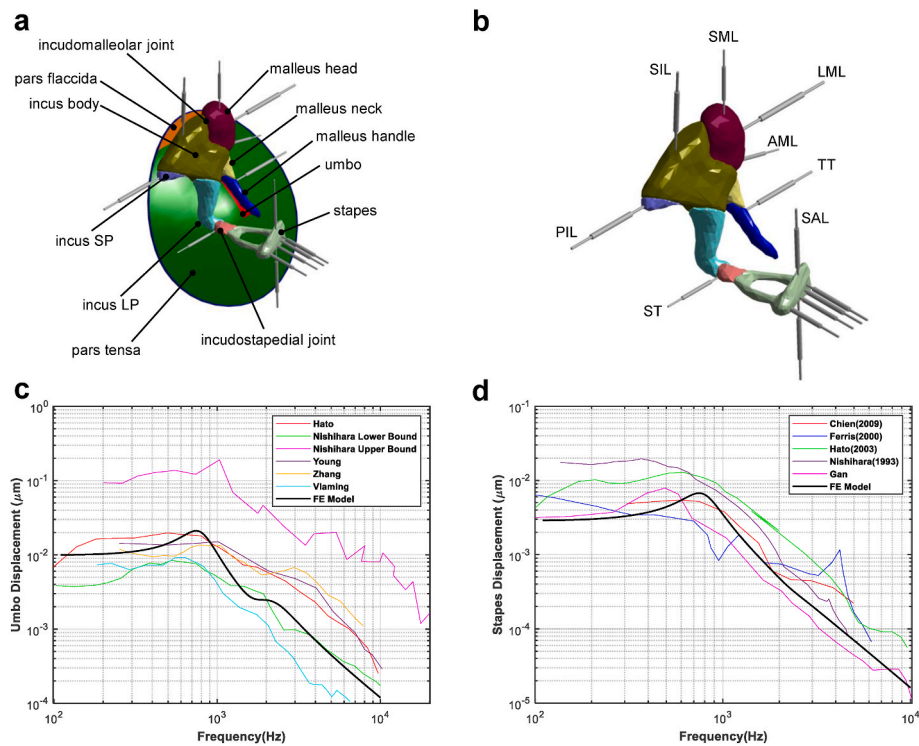
Fig. 2. FE model of human middle ear. (a) 3D geometry of human middle ear components in isometric view. (b) Spring boundary condition representation of ligaments, tendons, and impedance of cochlear fluid at stapes footplate. Note that the grey lines with thickened middles represent spring-dashpot system, as the combination of both stiffness and damping effects. (c) Comparison of umbo displacement between FE model and experimental data of (Hato et al., 2003; Nishihara and Goode, 1997; Vlaming and Feenstra, 1986; Young et al., 2010; Zhang et al., 2014). (d) Comparison of umbo displacement between FE model and experimental data of (Chien et al., 2009; Ferris and Prendergast, 2000; Gan et al., 2004; Hato et al., 2003; Nishihara et al., 1993).

2.5. MEMS fabrication of multimode piezoelectric sensor

Fabrication of the devices commenced on a 4-inch silicon-on-insulator (SOI) wafer with a 15 μm device layer, 500 μm handle layer, and 1 μm buried oxide layer. The detailed fabrication flow is presented in Fig. 5a. Initially, a 500 nm-thick silicon oxide was thermally grown on the top and bottom surfaces of the SOI wafer. Ti/Pt bimetallic layer (20 nm/100 nm) was sputtered as the bottom electrode layer. Then, thin film PLD PZT layer deposition was conducted at the MESA + Nano Lab. The PZT layer was patterned by a two-step wet etching recipe, in which consecutive immersions in $HF: HNO_3: NH_4OH: H_2O$ solution for etching and $HCl: H_2O$ for following residual removal were applied until the PZT layer was fully etched due to the differences in reaction rates of multiple elements. The bottom electrode was realized by etching Pt and Ti with hot Aqua Regia (3:1 $HCl: HNO_3$ at 60 °C) and diluted $HF: H_2O_2: H_2O$ solution, respectively (Koyuncuoğlu et al., 2022). Prior to the definition of the top electrode, a thin insulation layer of 1 μm-thick parylene-C layer was deposited with silane A-174 (PDS, 2010; SCS) to increase its adhesion and patterned by reactive ion etching (RIE) process. Following the insulation layer definition, top electrode metallization (Cr/Au, 20 nm/200 nm) and etching were performed after specifying pertaining regions with photolithography. Then, the remnant parylene on the wafers was entirely stripped by RIE using the top electrode pattern as a mask. The beams were formed via the frontside deep reactive ion etching (DRIE) process. Finally, beam release and mass formation were completed by processing the wafer from the backside using the DRIE process. The fabricated devices feature an overall footprint of 4.62 mm by 4.20 mm and weigh 3.6 mg. SEM images of the individual cantilevers are presented in Fig. 5b.

2.6. Electrical characterization of multimode piezoelectric sensor

Before the characterization step, electrical connections of the fabricated sensors were checked by performing a simple short test on each electrode pair using a digital multi-meter under an optical microscope. After ensuring fair electrical isolation, a commercial LCR meter (Agilent E4980A) was used to assess the existence of resonant frequencies for each channel. Frequency sweep measurements in the expected frequency range of the corresponding channel were carried out by applying 300 mV AC test voltage. The capacitance and resistance of metal/PZT/metal stacks were recorded with a sufficient sampling rate to isolate the resonance peaks (Fig. S3).

2.7. Mechanical characterization of multimode piezoelectric sensor

The experimental setup for the mechanical characterization of the devices is composed of a shaker table (B&K, vibration exciter type 4809), an accelerometer, a controller (Vibration Research VR-8500 shaker vibration control system), a power amplifier (B&K, Type 2718 power amplifier), and a data acquisition (DAQ) board (NI Compact DAQ). During the experiments, the sensor was placed in a chip holder, which allows direct electrical connections between channels and the DAQ board using jumper wires. The transducer was clamped to the shaker, driven by the power amplifier through the Vibration VIEW software. The acceleration input was regulated via a closed-loop system between the vibration controller and the accelerometer. The piezoelectric responses of each channel were acquired by the DAQ board using the graphical programming environment LabView in automation. The cantilevers were vibrated by a periodic chirp signal having frequencies ranging from 300 Hz to 6 kHz under 0.1 g acceleration. According to the cadaver experiment, the given acceleration of 0.1 g corresponds to a resultant vibration amplitude of 100 dB SPL at 500 Hz.

2.8. Acoustic characterization of multimode piezoelectric sensor

The acoustic characterization of the piezoelectric vibration sensors incorporates a PDMS artificial tympanic membrane to mimic the vibration response of middle ear components (Ashrafi et al., 2018). The experimental setup is composed of a signal generator (KEYSIGHT Waveform Generator 33600 A), a stereo amplifier (Denon-PMA-520AE), a dB meter, an ER2 insert microphone (Etymotic), a DAQ board (NI Compact DAQ) and an acoustic holder (Fig. 6a). A sinusoidal test signal was generated by the signal generator and the acoustic output is generated by ER2 insert microphone. The amplitude of the signal was regulated with the dB-meter and the amplifier. The generated acoustic input excites the artificial membrane, which triggers the piezoelectric sensor to vibrate. The data acquisition was carried out using the same procedure as the experimental setup for the mechanical characterization. The experiment is executed from 50 dB SPL to 100 dB SPL with 10 dB steps.

3. Results and discussion

3.1. Cross-calibration and validation of the FE model

In order to fit the vibration characteristics of the developed FE Model, a cross-calibration approach was implemented. This approach compares umbo and stapes displacements of the FE model and the experimental data derived from human temporal bones. It reduces the possible disparities by tuning the unspecified FE model parameters, including spring constants. For the cross-calibration process, harmonic analysis was carried out with ANSYS using a uniform harmonic pressure stimulus to the lateral side of the TM. The material parameters for the model are provided in Table S1. The resulting model includes 41365 elements and 79255 nodes. The maximum mesh size used in the FE simulations is orders of magnitude smaller than the deformation waves propagating in the ear bones and tissue. The final parameters for ligaments and tendons are provided in Table S2.

The validation process was done through an investigation of the vibration characteristics at the endpoints of the developed model. The accuracy of the FE model was assessed by examining the vibration behaviors both at the stapes footplate (terminal end of the middle ear) and the umbo, which lies at the entry to the middle ear. The frequency responses of umbo and stapes footplate displacement are demonstrated in Fig. 2c and d, together with the experimental data reported in the literature for 80 dB SPL spanning from 100 Hz to 10 kHz. As observed from the figure, umbo displacement amplitudes from experimental data of various studies ranged between a lower (0.2 nm) and an upper bound (40 nm) over the frequency range of 100 Hz to 10 kHz (Nishihara and Goode, 1997). The simulation result of the FE model yielded an umbo displacement amplitude between 0.2 and 10 nm, which varied with the frequency and was consistent with the lower and upper bound. In the case of stapes, the simulation results were exhibited displacement amplitude values between 0.02 and 3 nm over the frequency range of 100 Hz to 10 kHz, which showed an excellent consistency with the previous studies (Hato et al., 2003; Nishihara and Goode, 1997; Young et al., 2010; Zhang et al., 2014; Vlaming and Feenstra, 1986).

3.2. Cadaveric feasibility study of middle ear implantation

A cadaveric experiment was performed to assess the feasibility of attaching the titanium coupler to the incus SP and ensuring a sufficiently rigid connection. In this study, a commercial accelerometer was affixed onto the coupler to collect precise vibration data from the incus. The backplate of the coupler serves as the platform for the sensor, and the coupler is securely affixed to the ossicles on its opposite side. In the context of this feasibility study, an accelerometer, sharing comparable dimensions with the designated sensor, is employed. The validation of the successful coupling is achieved by collecting vibration data from all three motion axes.

The incus SP functions as a strategic anchoring point for clamping due to its posterior location, facilitating easy accessibility through a relatively simple mastoidectomy, as demonstrated in this paper to access the middle ear cavity. This decision is supported by empirical evidence demonstrating reduced surgical procedure time and minimized risks, such as facial nerve palsy and severed chorda tympani (Schraven et al., 2018). Surgical outcomes validate the advantages of the SP coupler, with significantly faster implantation procedures compared to vibroplasty by crimping, leading to shorter hospital stays (Lee et al., 2017; Schraven et al., 2018). These findings collectively highlight the efficacy of utilizing the incus SP for coupler implantation, supported by both surgical efficiency and comparable audiometric outcomes. Furthermore, the coupler can be attached by sliding it without the need for crimping owing to our coupler design, while the transducer is attached to the confronting back plate.

The cadaver experiment was conducted to validate the feasibility of the coupler design, including implantation and the developed 3D FE model of the middle ear. Under an optical microscope, the suitability of the coupler as an attachment apparatus for FICI applications in terms of dimensions and easiness of surgical operations was observed (Fig. 3a). Fig. 3b illustrates the implanted commercial accelerometer via the fabricated titanium coupler, providing the indications of the three motion axes. The Ansys modal analysis for the titanium coupler reveals that all resonance frequencies exceed the desired 6 kHz threshold, where the first natural resonances observed at 8.9 kHz even for the case of a mass loading of 30 mg to ensure effective vibration transfer.

An acoustic wave with amplitudes ranging from 80 dB SPL to 100 dB SPL was applied, and the response was captured within the range of 200 Hz–800 Hz. Fig. 3c illustrates the time-dependent acceleration measurement results at all three axes. The mass loading effect of the coupler was also investigated through FEM simulations. For that purpose, a 25 mg mass, closely matching the total implanted mass, was attached to the incus SP and the displacement for an input between 80 and 100 dB input was obtained for the frequencies between 100 Hz and 1 kHz. Vibration data from incus SP together with FE model data under mass loading of the implanted accelerometer via the titanium coupler is depicted in terms of acceleration for SPL of 80 dB–100 dB in Fig. 3d. The FE model for 80, 90, 100 dB SPL shows a good consistency by having correlation coefficient (R^2) of 0.97. Notably, the vibration amplitude for incus can vary up to 10 times for different cadavers (Djinovic et al., 2020); thus, the correlation is acceptable.

Moreover, a resultant acceleration amplitude of 0.1 g is measured for a 100 dB SPL stimulus at 500 Hz. The measurement of the acceleration levels during the initial cadaveric experiment also serves as a fundamental parameter for the design of the piezoelectric sensor. The sensor should be engineered to generate a significant voltage output corresponding to the available acceleration levels. The acceleration response aligned with the z-axis is observed to be less than half of the responses along the other axes. As the sensor attachment surface of the coupler lies in the XY plane, adjustments to rotate the coupler surface are necessary within the available space to maximize excitation (resultant force) on the sensor structure during implantation. This ensures optimal sensor performance aligned with the orientation constraints of the attachment surface. Future cadaveric studies should delve deeper into the alignment considering available space and sensor dimensions for enhanced vibration transfer.

3.3. Optimization of band coverage of multimode piezoelectric sensor

Optimization of the MEMS sensor for obtaining enhanced operation frequency range and dynamic range was achieved via the FEM simulations by tuning the dimensions of the cantilevers. In FEM simulations, two primary studies were conducted: modal analysis and frequency response function analysis (FRF). Parametric sweeps were applied to investigate the system behavior by coupling structural and electrical
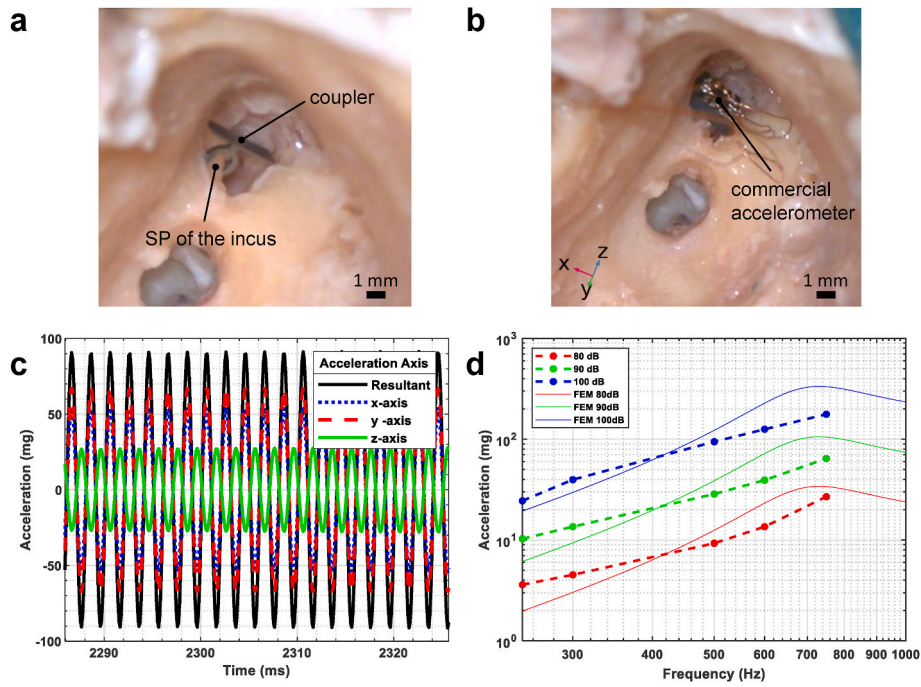
Fig. 3. The implementation and evaluation of the cadaveric experiment. (a) Manufactured Ti-Gr5 coupler crimped to the incus SP at cadaver experiment. (b) Illustration of the commercial accelerometer implanted through the titanium coupler. (c) Time dependent vibration amplitude of the incus SP obtained by the commercial accelerometer. (d) Cadaver experiment results from incus SP and FE results under 25 mg mass loading for 250 Hz–1000 Hz from 80 dB to 100 dB SPL (The presented acceleration values represent the resultant 3D motion).
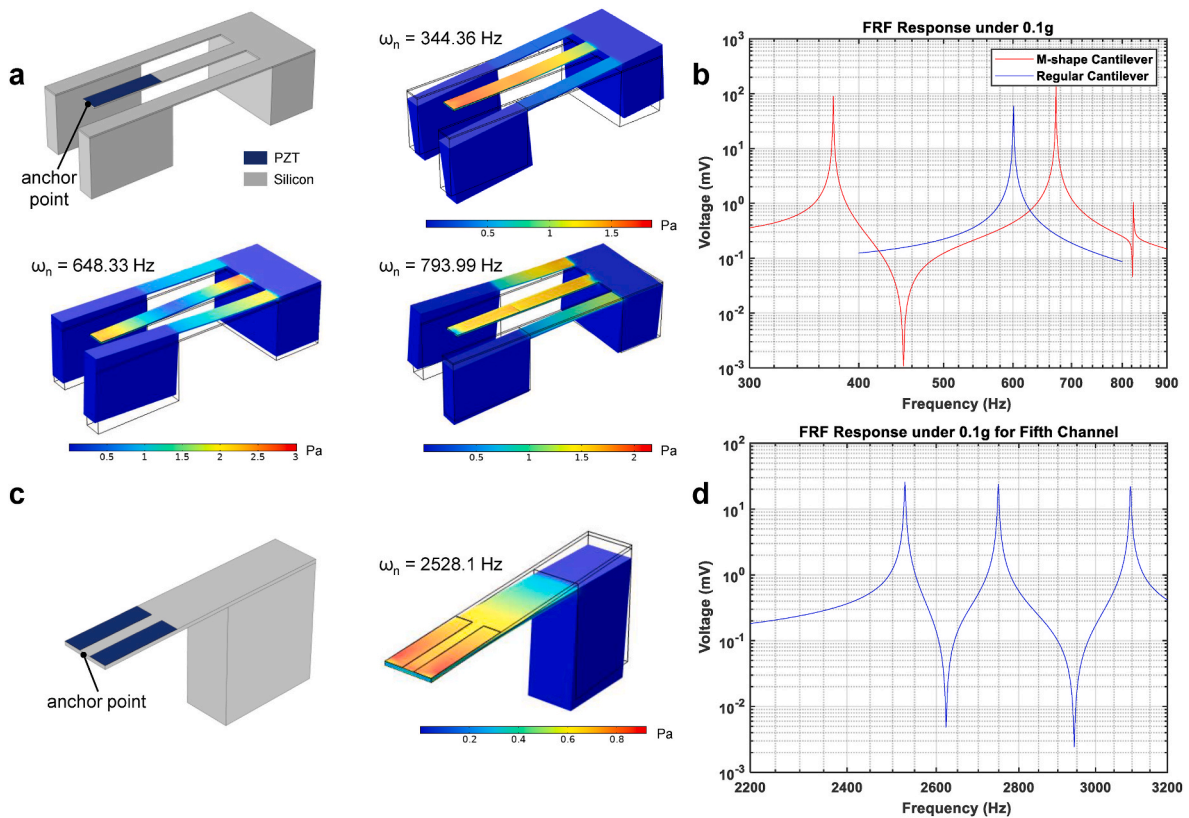

Fig. 4. The simulation regarding vibration modes. (a) Illustration of a multimodal M-shaped cantilever (the first channel) and simulations depicting its three bending modes under the condition of one end being anchored, accompanied by the Von Mises stress distribution. (b) Comparative analysis of FRF results of multimode and single mode cantilever for the first channel definition. (c) Single cantilever with serially connected double patched PZT illustration and initial bending mode under the condition of one end being anchored, accompanied by the Von Mises stress distribution. (d) FRF analysis result of the fifth channel.

domains to optimize broadband operation for the dimensional variations in beam width, beam lengths, tip mass, and piezo material. The single-mode cantilever consists of a serially connected double PZT layer to enhance its performance. The 3-mode asymmetric M-shaped cantilever consists of a main beam and two folded auxiliary beams with corresponding dimensions to arrange their resonance (Fig. 4a). The thicknesses of the silicon beam and the tip mass were specified as 15 μm and 500 μm, respectively, and thickness of the PLD PZT was specified as 1 μm. Material properties of the piezoelectric material are presented by Table S6.

Modal analysis of single and multimode cantilevers was performed for tuning resonance frequency distribution. During the modal analysis, three bending modes were observed due to the asymmetric design, all of which induce stress on the PZT patches placed onto the main beam

structure, resulting in voltage output generation (Fig. 4a). Resonance frequencies for the first M-shape cantilever were acquired as 344.36 Hz, 648.33 Hz, and 793.99 Hz, respectively, for its first three bending modes. It was also observed from Fig. 4a that the maximum stress distribution over the cantilevers occurs at the anchor points on the PZT layer, as expected. The voltage response plot (Fig. 4b) reveals distinct regions of diminished voltage outputs between consecutive resonances, which can be attributed to the antiresonance phenomenon. Despite missing data at certain frequencies, the multimodal cantilever surpasses the single-mode one of similar beam width by offering enhanced frequency information through its capacity to encompass a broader sensitivity range across multiple resonance modes, thus contributing to an enriched frequency analysis and improved overall performance. A numerical comparison between a three-mode multimodal cantilever and a
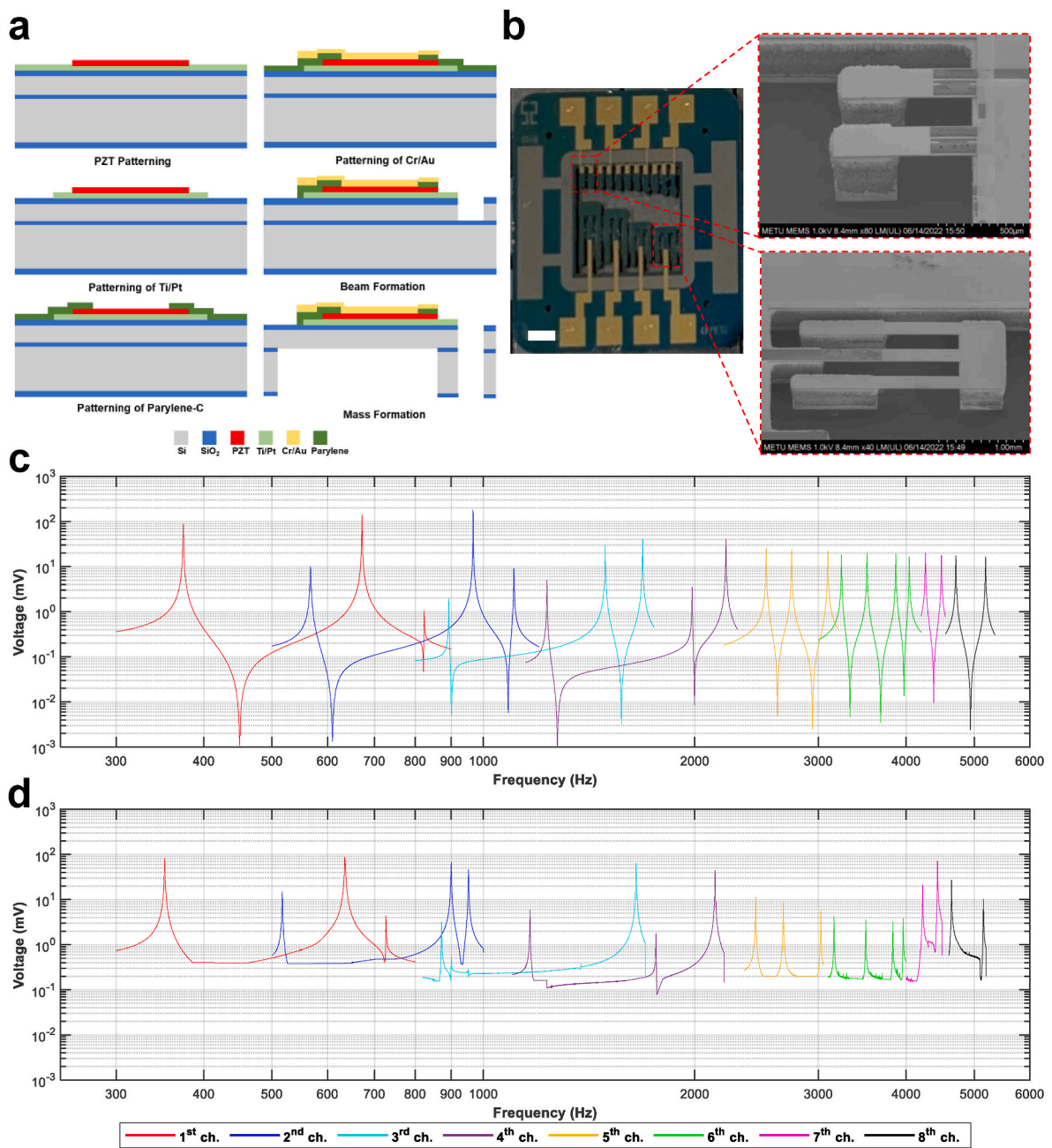

Fig. 5. The fabrication, design and mechanical characterization of the multimode multichannel piezoelectric sensor. (a) The sequence for the fabrication process flow. (b) The fabricated piezoelectric sensor and closed-up SEM images of the cantilevers. Scale Bar: 1.1 mm. (c–d) Numerical (top) and experimental (bottom) FRF results of the M-shape device under 0.1 g acceleration from 300 Hz to 6 kHz.
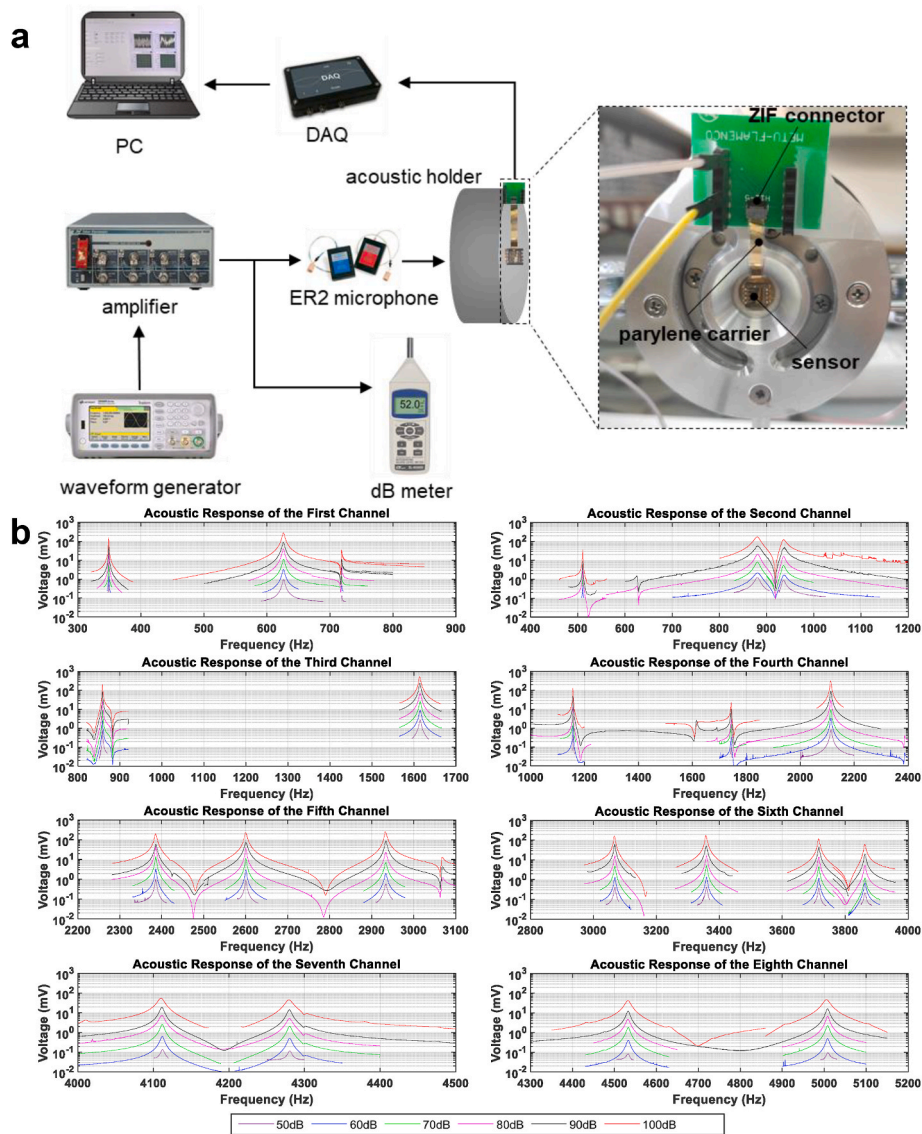
Fig. 6. Acoustic characterization of piezoelectric sensor using artificial tympanic membrane. (**a**) A schematic view of an experimental setup and SEM images of the fabricated sensor (Scale Bar: 1 mm). The fabricated multimode multichannel sensor was assembled with an artificial tympanic membrane which was placed onto the acoustic holder. When acoustic input was applied via the ER2-insert microphone, sensor generates a piezoelectric output which was collected with DAQ. (b) Acoustic responses of 8-channel sensor from 50 dB to 100 dB SPL.

single mode cantilever can be accomplished by calculating numerical cumulative voltage response, the integral of the spectral voltage response within the desired channel frequency range. The calculated ratio of 2.05, representing the comparison of two areas, denotes a higher cumulative voltage response, implying an increased capture of frequency information and enhanced sensitivity in the multimodal sensor. In comparison with a conventional single-mode linear cantilever beam (the length of 2.7 mm), the M-shape structure also offers a reduced beam length of 2.5 mm, which is essential to define an appropriate device size fitting inside the middle ear, despite the existence of a lower frequency resonance point.

The utilization of multimodal M-shape cantilevers was beneficial up to 2.5 kHz for the first resonance frequency. Above that frequency, the second and third modes do not fall in the desired operation range (300 Hz-6 kHz); consequently, conventional single-mode cantilever structures were preferred to collect the remaining range. The performance of the single-mode cantilevers was enhanced by dividing and connecting PZT layers serially to obtain higher voltage output. Moreover, individual beams are interconnected in a serial manner, forming a single channel.

Fig. 4c and d presents the bending mode of a single cantilever with a resonance frequency of 2528.1 Hz and the voltage response plot of the serially connected cantilever array, which defines the fifth channel.

To this end, in the final sensor design, four multimode M-shape cantilever structures were employed for sensing the range up to 2.5 kHz; and 11 single-mode cantilever structures were preferred in a serially connected configuration for the remaining interval up to 6 kHz (Fig. S2). A total number of 8 channels was defined to capture all 23 modes. After tuning resonant frequencies using modal analysis, the frequency response of the piezoelectric sensor at 0.1 g acceleration was obtained. It should be noted that 0.1 g acceleration refers to 100 dB SPL at 500 Hz according to the cadaver experiment mentioned in Section 3.3. Spacing between output voltage waveforms from individual channels should be minimized in order to cover the whole frequency band considering. The acoustic band was covered when the resonant frequencies of all relevant 23 modes were systematically arranged to cover between 300 Hz and 6 kHz at a given acceleration level of 0.1 g via the superposition of resonances of all eight channels. The resonance peaks of each mode are considerably separated from each other. It can be seen from Fig. 5c that

the frequencies around anti-resonances have small voltage amplitudes. At these low voltage output frequencies for a particular channel, the response of another channel contributes with a higher voltage amplitude above the threshold voltage. With this strategy, the sensor output regions below the threshold voltage are minimized for a wide frequency band.

3.4. Characterization of multimode piezoelectric sensor

As aforementioned, the characterization of the fabricated sensor was assessed by examining the electrical, mechanical, and acoustic responses. In the case of electrical characterization, resonance frequencies of each channel were obtained through the capacitance (C) and resistance (R) measurements (Fig. S2). The multiple resonance peaks were observed for the first channel as a result of the multimode effect.

Afterward, the mechanical characterization was assessed with the shaker table by investigating the piezoelectric response under 0.1 g acceleration. Piezoelectrical responses of the channels as output voltage waveforms were presented in Fig. 5d. The multimode effect was achieved through the continuous waveforms having a total of 22 resonance peaks acquired from 8 channels. A possible explanation for the absence of a resonance peak at the third channel could be the overlapping of two consecutive modes due to the presence of deviations or inaccuracies during the fabrication process. The empirical piezoelectric response results exhibit good accuracy with the simulation data (Fig. 5d) regarding the magnitudes and the locations of resonance peaks (Table S3). According to the vibration measurements, resonance peak locations were coherent with modal analysis simulations with a maximum deviation of 88.3% per channel, demonstrating the accuracy of the microfabrication process and the FEM simulations.

In the acoustic characterization, the middle ear environment was mimicked by attaching the sensor to the polydimethylsiloxane (PDMS) artificial tympanic membrane. An artificial membrane construction is particularly significant because it shows similar physical and spatial characteristics with the tympanic membrane (Yuksel et al., 2022). Acoustic characterization was acquired by observing the performance of the sensor on the membrane in terms of output voltage signals for each channel. The results of the acoustic experiments are depicted in Fig. 6b and Fig. S3 in the supplementary information document.

Acoustic characterization results showed that (Fig. 6b) all cantilevers exhibit resonance responses at all SPL levels, and thus, the proposed multimode multichannel device detects most of the speech frequency range (300 Hz - 6 kHz) along with acoustic pressure amplitudes relevant to daily hearing-related activities (50 dB–100 dB). The piezoelectric response of the device generates an output voltage signal in the range of 1–100 mV for the corresponding frequency range of 300 Hz to 6 kHz at 90 dB SPL. Under an acoustic excitation at 100 dB SPL, an output voltage of up to 546.16 mVpp was generated for 600 kΩ load resistance. This output voltage value is noteworthy since it is at least threefold higher than what has been reported in previous studies with similar experimental setups (Ilik et al., 2018; Jang et al., 2015; Udvardi et al., 2017; Yuksel et al., 2022). Moreover, owing to the multimode effect of the sensor, almost the whole audio spectrum was covered between 300 Hz and 6000 Hz at 90 dB SPL. Even at 50 dB SPL input stimulus, 22 resonant peaks were observed, which indicates the wide dynamic frequency range of the piezoelectric sensor between 300 Hz and 6000 Hz. It is also noteworthy that the sensor exhibits linear behavior at its resonance frequencies, demonstrating a proportional relationship between the input sound pressure and the corresponding voltage output. The maximum achieved sensitivity of the sensor was 285.28 mVpp/Pa at 1613 Hz, which was a 10-fold improvement compared to our previous study (Yuksel et al., 2022). The elaborated results regarding generated voltage output and sensitivities of each mode are provided in Table S4.

For good measure, the extrapolated results indicate that, even at 30 dB SPL (whisper level), the sensor generated an output voltage ranging from 7 to 180 μV at resonance peaks. These voltage levels are sufficiently

high to operate a neural stimulation interface circuit implemented as a FICI concept, because each channel provides a more substantial output voltage than the expected input-referred noise of a low-noise interface circuit (Yip et al., 2015). Since the sensor captures enhanced speech information from multichannel and multimodal signals spanning the targeted frequency range, it has the merit of functional signal selection with a filter bank for neuro-stimulation at the electrode-neural interface for improved speech perception. Table 1 compares our sensor and similar studies by assessing the key parameters, including geometry, material, minimum detectable signal, and operating frequency range. Our design stands out with its multimodal structure, wide range of operation frequency, and perceptible signal amplitude. Consequently, our MEMS-based sensor demonstrates significant promise for FICI applications.

4. Conclusion

This paper studied designing and implementing an implantable MEMS-based multimodal multichannel piezoelectric vibration transducer to detect the sound-induced ossicular motion inside the middle ear. The transducer, implantable into the middle ear with a uniquely designed titanium coupler, incorporates 4 M-shape multimode cantilevers and 11 serially connected single-mode cantilevers. An FE model of the middle ear was constructed to evaluate the incus SP as the insertion location of the coupler for attaching the transducer unit, considering the resultant vibration. The assessment of vibration response measurements from the human cadaveric middle ear validates the accuracy of the middle ear FE model under 1 kHz. Thus, the collected acceleration data assisted in the design of the transducer unit. The detection performance of the sensor was demonstrated between 50 dB and 100 dB SPL with a hearing-relevant frequency band of 300–6000 Hz by utilizing an artificial tympanic membrane as a proof-of-concept study to exhibit the applicability of the intended implantation. The multimodal, multichannel cantilever array mimics the tonotopic characteristics of the middle ear. It overcomes the limitations of state-of-the-art devices by extending the frequency range, improving the dynamic range, lowering device mass, and decreasing the footprint.

Fully implantable cochlear implants represent a significant advance over conventional methods, not only technologically, but also in terms of improving the patient's quality of life. Compared to traditional cochlear implants that require external components such as microphones, speech processors, and transmitters, fully implantable systems eliminate the need for bulky external devices. This improves the patient's overall experience by providing greater comfort, aesthetics, and protection from environmental elements. In addition, fully implantable cochlear implants have the potential to leverage the natural hearing mechanism, including the vibration of the ossicular chain in the middle ear, as well as the outer ear (pinna) and ear canal (Calero et al., 2018). By preserving these natural components of hearing, fully implantable devices have the potential to improve speech perception compared to traditional cochlear implants that bypass these structures entirely.

However, it is crucial to address the risks associated with fully implantable cochlear implants, such as potential damage to the ossicular chain during surgical implantation. Damage to these delicate structures can lead to hearing loss or other complications for the patient. Careful surgical techniques and precise implant placement are essential to reduce these risks. Surgeons undergo extensive training and use advanced imaging technologies to ensure safe and accurate placement while minimizing the risk of damage to surrounding structures (Eastwood et al., 2021). In addition, continuous monitoring and follow-up care are required to promptly detect and address potential problems. Despite these risks, the benefits of fully implantable cochlear implants in terms of comfort, aesthetics, and potential improvements in speech perception make them a promising option for individuals with hearing loss.

Moreover, for practical implementation of a multimodal and

Table 1
Summary of state of art implantable auditory sensors.

Study	Concept	Geometry	Material	SPL (tested)	Frequency Range	Disadvantage
Jang et al. (2015)	Artificial Basilar Membrane	8 - regular cantilever array	AlN	70 dB	2.9 kHz – 12.6 kHz	· Inferior low frequency selectivity · Large footprint · Signal processing
Zhao et al. (2019)	Piezoelectric Transducer	4 - regular cantilever array	AlN	80 dB	1 kHz – 14 kHz	· Inferior low frequency selectivity · Signal processing
Young et al. (2012)	Capacitive Accelerometer	Comb structure	NA	35 dB	500 Hz – 8 kHz	· Inferior low frequency selectivity · Power consumption
Beker et al. (2013)	Piezoelectric Transducer	Cantilever	PZT (Bulk)	NA	500 Hz – 2.5 kHz	· Narrow bandwidth
Ko et al. (2009b)	Capacitive Displacement Sensor	Diaphragm	NA	40 dB	600 Hz – 8 kHz	· Inferior low frequency selectivity · Power consumption
Jia et al. (2016)	Floating Microphone	Bimorph element	PZT	50 dB	100 Hz – 10 kHz	· Excess mass (67 mg)
(Gesing et al., 2018)	Piezoelectric Transducer	Annular diaphragm	AlN	60 dB	600 Hz – 10 kHz	· Inferior low frequency selectivity · Excitation above normal speech
Yuksel et al. (2022)	Piezoelectric Transducer	8 - regular cantilever array	PZT	50 dB	250 Hz – 5.5 kHz	· Inferior sensitivity · Signal processing
Current Study	Piezoelectric Transducer	Multimode cantilever array	PZT	50 dB	300 Hz – 6 kHz	· Complexity in design · Signal processing

multichannel piezoelectric transducer, it is essential to address a unique challenge posed by its operation, characterized by multiple resonance peaks. This necessitates the development of sound level adjustment techniques to accommodate the varied amplitudes of each resonance in response to acoustic excitation. Here, circuit architectures for piezoelectric shunt damping could be adapted for multimodal vibration control and mitigation (Raze et al., 2022).

To ensure mechanical integrity within the middle ear, packaging of the sensor is imperative. Further exploration of robust 3D packaging solutions is recommended to enhance the long-term performance of the implant. The eventual goal of a completely implantable CI with no visible components will require the development of a wireless interface for transmitting enough power to the implanted rechargeable battery in an acceptable timeframe. Ongoing research involves the development of a novel triple-mode rectifier circuit operating at 13.56 MHz, capable of wirelessly powering medical implants by adjusting its operation mode based on the received signal voltage level, achieving an extended input power range and output power range from 0.233 to 51.54 mW (Engur et al., 2021). Additionally, the advances in the efficiency of microelectronics and the research on novel piezoelectric materials could lead the system to be fed by a separate piezoelectric energy scavenging unit. The transducer unit and the design and characterization methodology proposed in this paper serve as a milestone and could offer an intriguing approach to the realization of next-generation FICI systems and other auditory prostheses.

CRediT authorship contribution statement

Feyza Pirim: Writing – review & editing, Writing – original draft, Visualization, Validation, Methodology, Investigation, Formal analysis, Data curation, Conceptualization. **Ali Can Atik:** Writing – review & editing, Writing – original draft, Visualization, Validation, Methodology, Investigation, Formal analysis, Data curation. **Muhammed Berat Yüksel:** Validation, Methodology, Investigation, Formal analysis, Data curation. **Akın Mert Yılmaz:** Validation, Investigation, Data curation. **Mehmet Birol Uğur:** Validation, Investigation. **Selçuk Tunalı:** Validation, Investigation. **Aykan Batu:** Supervision. **Mahmut Kamil Aslan:** Writing – review & editing, Writing – original draft, Visualization, Supervision. **Mehmet Bülent Özer:** Writing – review & editing, Writing – original draft, Supervision. **Haluk Külah:** Writing – review & editing, Writing – original draft, Validation, Supervision, Project administration, Funding acquisition.

Declaration of competing interest

The authors declare that they have no known competing financial interests or personal relationships that could have appeared to influence the work reported in this paper.

Data availability

Data will be made available on request.

Acknowledgement

Appendix A. Supplementary data

Supplementary data to this article can be found online at https://doi.org/10.1016/j.biosx.2024.100471.

References

Beker, L., Zorlu, Ö., Goksu, N., Kulah, H., 2013. Transducers &Eurosensors XXVII, 1663–1666.

Beutner, D., Hüttenbrink, K.B., 2009. German society of Oto-Rhino-Laryngology. Head Neck Surg. 88, 32–47.

Calero, D., Paul, S., Gesing, A., Alves, F., Cordioli, J.A., 2018. Biomed. Eng. Online 17 (1), 23.

Campanella, H., Camargo, C.J., Lopez Garcia, J., Daza, A., Urquiza, R., Esteve, J., 2012. J. Microelectromech. Syst. 21, 1452–1463.

Chadha, S., Kamenov, K., Cieza, A., 2021. Bull. World Health Organ. 99, 242-242A.

Chen, F., Cohen, H.I., Bifano, T.G., Castle, J., Fortin, J., Kapusta, C., Mountain, D.C., Zosuls, A., Hubbard, A.E., 2006. J. Acoust. Soc. Am. 119, 394–405.

Chien, W., Rosowski, J.J., Ravicz, M.E., Rauch, S.D., Smullen, J., Merchant, S.N., 2009. Hear. Res. 249, 54–61.

Dahroug, B., Tamadazte, B., Weber, S., Tavernier, L., Andreff, N., 2018. IEEE Rev Biomed Eng 11, 125–142.

Djinovic, Z., Tomic, M., Pavelka, R., Sprinzl, G., Traxler, H., 2020. IEEE 1894–1898.

Eastwood, M., Biggs, K., Metcalfe, C., Muzaffar, J., Monksfield, P., Bance, M., 2021. J Int Adv Otol 17 (2), 162–174.

Engur, Y., Yigit, H.A., Kulah, H., 2021. IEEE Trans Biomed Circuits Syst 15, 68–79.

Ferris, P., Prendergast, P., 2000. J. Biomech. 33, 581–590.

Gan, R.Z., Wood, M.W., Dyer, R.K., Dormer, K.J., 2001. Ann. Otol. Rhinol. Laryngol. 110, 478–485.

Gan, R.Z., Feng, B., Sun, Q., 2004. Ann. Biomed. Eng. 32, 847–859.

Gan, R.Z., Reeves, B.P., Wang, X., 2007. Ann. Biomed. Eng. 35, 2180–2195.

Gesing, A.L., Alves, F.D.P., Paul, S., Cordioli, J.A., 2018. Sci. Rep. 8, 3920.

Graf, L., Lochner, J., Mojallal, H., Arnold, A., Honegger, F., Stieger, C., 2023. Int. J. Audiol. 62, 192–198.

Guan, Q.C., Ju, B., Xu, J.W., Liu, Y.B., Feng, Z.H., 2013. J. Intell. Mater. Syst. Struct. 24, 1059–1066.

Harne, R.L., Sun, A., Wang, K.W., 2016. J. Sound Vib. 363, 517–531.

Hato, N., Stenfelt, S., Goode, R., 2003. Audiol. Neurootol. 8, 140–152.

Huang, X., Zhang, C., Dai, K., 2021. Micromachines 12, 203.

İlik, B., Koyuncuoğlu, A., Şardan-Sukas, Ö., Külah, H., 2018. Sens Actuators A Phys 280, 38–46.

Jang, J., Kim, S., Sly, D.J., O'leary, S.J., Choi, H., 2013. Sens Actuators A Phys 203, 6–10.

Jang, J., Lee, J., Woo, S., Sly, D.J., Campbell, L.J., Cho, J.-H., O'Leary, S.J., Park, M.-H., Han, S., Choi, J.-W., Hun Jang, J., Choi, H., 2015. Sci. Rep. 5, 12447.

Jia, X.-H., Gao, N., Xu, X., Wu, Y.-Z., Kang, H.-Y., Chi, F.-L., 2016. Acta Otolaryngol. 136, 1248–1254.

Ko, W.H., Zhang, R., Huang, P., Guo, J., Ye, X., Young, D.J., Megerian, C.A., 2009a. IEEE Trans Biomed Circuits Syst 3, 277–285.

Ko, W.H., Zhang, R., Huang, P., Guo, J., Ye, X., Young, D.J., Megerian, C.A., 2009b. IEEE Trans Biomed Circuits Syst 3, 277–285.

Koyuncuoğlu, A., Işık Akçakaya, D., Şardan Sukas, Ö., Külah, H., 2022. Micro and. Nano Engineering 16, 100153.

Leadenham, S., Erturk, A., 2014. J. Sound Vib. 333, 6209–6223.

Leadenham, S., Erturk, A., 2015. Smart Mater. Struct. 24, 055021.

Lee, H.S., Chung, J., Hwang, G.-T., Jeong, C.K., Jung, Y., Kwak, J.-H., Kang, H., Byun, M., Kim, W.D., Hur, S., Oh, S.-H., Lee, K.J., 2014. Adv. Funct. Mater. 24, 6914–6921.

Lee, J.M., Lee, Y.H., Jung, J., Kim, S.H., Moon, I.S., Choi, J.Y., 2017. Otol. Neurotol. 38 (8), 1063–1070.

Levy, S.C., Freed, D.J., Nilsson, M., Moore, B.C.J., Puria, S., 2015. Ear Hear. 36, e214–e224.

Liem, T., 2004. In: Liem, T.B.T.-C.O. (Ed.), Chapter 17 - the Organ of Hearing and Balance, Second E. Churchill Livingstone, Edinburgh, pp. 605–633.

Liu, D., Al-Haik, M., Zakaria, M., Hajj, M.R., 2018. J. Intell. Mater. Syst. Struct. 29, 1206–1215.

Masara, D.O., El Gamal, H., Mokhiamar, O., 2021. Energies 14.

Nabavi, S., Zhang, L., 2017. 2017, Paris, France, 3–6 September 2017. MDPI, p. 586.

Nabavi, S., Zhang, L., 2019. IEEE Sensor. J. 19, 4837–4848.

Nishihara, S., Goode, R.L., 1997. Proc Internat Workshop Middle-Ear Mech Res Otosurg. (Germany), Dresden, pp. 91–93.

Nishihara, S., Aritomo, H., Goode, R.L., 1993. Otolaryngology-Head Neck Surg. (Tokyo) 109, 899–910.

Puria, S., Fay, R.R., Popper, A.N., 2013. The Middle Ear: Science, Otosurgery, and Technology. Springer Science, New York.

Raze, G., Dietrich, J., Lossouarn, B., Kerschen, G., 2022. Mech. Syst. Signal Process. 176, 109120.

Rusinek, R., 2021. Eur. J. Mech. Solid. 85, 104068.

Saunders, J.E., Francis, H.W., Skarzynski, P.H., 2016. Otol. Neurotol. 37, e135–e140.

Schraven, S.P., Mlynski, R., Dalhoff, E., Heyd, A., Wildenstein, D., Rak, K., Radeloff, A., Hagen, R., Gummer, A.W., 2016. Hear. Res. 340, 179–184.

Shintaku, H., Nakagawa, T., Kitagawa, D., Tanujaya, H., Kawano, S., Ito, J., 2010. Sens Actuators A Phys 158, 183–192.

Sun, S., Tse, P.W., 2019. Mech. Syst. Signal Process. 114, 467–485.

Sun, Q., Gan, R.Z., Chang, K.-H., Dormer, K.J., 2002. Biomech. Model. Mechanobiol. 1, 109–122.

Udvardi, P., Radó, J., Straszner, A., Ferencz, J., Hajnal, Z., Soleimani, S., Schneider, M., Schmid, U., Révész, P., Volk, J., 2017. Micromachines 8, 311.

Vlaming, M.S.M.G., Feenstra, L., 1986. Clin. Otolaryngol. 11, 411–422.

Vu, N.B., Truong, N.H., Dang, L.T., Phi, L.T., Ho, N.T.-T., Pham, T.N., Phan, T.P., Pham, P.V., 2016. Biomed Res Ther 3, 14.

Wilson, B.S., Dorman, M.F., 2008. Hear. Res. 242, 3–21.

Wu, M., Ou, Y., Mao, H., Li, Z., Liu, R., Ming, A., Ou, W., 2015. AIP Adv. 5, 77149.

Wyatt, J.R., Niparko, J.K., Rothman, M.L., deLissovoy, G., 1995. Am. J. Otol. 16, 52–62.

Yip, M., Jin, R., Nakajima, H.H., Stankovic, K.M., Chandrakasan, A.P., 2015. IEEE J Solid-State Circuits 50, 214–229.

Young, D.J., Zurcher, M.A., Trang, T.T., Megerian, C.A., Ko, W.H., 2010. Ear Nose Throat J. 89, 21–26.

Young, D.J., Zurcher, M.A., Semaan, M., Megerian, C.A., Ko, W.H., 2012. IEEE Trans. Biomed. Eng. 59, 3283–3292.

Yuksel, M.B., Koyuncuoglu, A., Kulah, H., 2022. IEEE Sensor. J. 22, 3052–3060.

Zhang, X., Guan, X., Nakmali, D., Palan, V., Pineda, M., Gan, R.Z., 2014. Journal of the Association for Research in Otolaryngology 15, 867–881.

Zhao, F., Koike, T., Wang, J., Sienz, H., Meredith, R., 2009. Med. Eng. Phys. 31, 907–916.

Zhao, C., Knisely, K.E., Colesa, D.J., Pfingst, B.E., Raphael, Y., Grosh, K., 2019. Sci. Rep. 9, 3711.

Zhao, Y., Yan, J., Cheng, J., Fu, Y., Zhou, J., Yan, J., Guo, J., 2023. IEEE Sensor. J. 1-1.

Zurcher, M., Young, D., Semaan, M., Megerian, C., 2006. Eng Med Biol Soc.,539-42. 539–542.